C Journal of Carbon Research

MDPI

Article

Evaluation and Optimization of Tour Method for Synthesis of Graphite Oxide with High Specific Surface Area

Hanna Bukovska [1,*], Fernando García-Perez [1], Natalia Brea Núñez [2], Laura J. Bonales [3], Andrés Velasco [4,5], M. Ángeles Clavero [1], Javier Martínez [4,6], Alberto J. Quejido [1], Isabel Rucandio [1] and M. Belén Gómez-Mancebo [1,*]

1 Technology Department, CIEMAT (Centro de Investigaciones Energéticas, Medioambientales y Tecnológicas), 28040 Madrid, Spain; fernando.garcia@ciemat.es (F.G.-P.); ma.clavero@ciemat.es (M.Á.C.); alberto.quejido@ciemat.es (A.J.Q.); isabel.rucandio@ciemat.es (I.R.)
2 Environmental Department, CIEMAT (Centro de Investigaciones Energéticas, Medioambientales y Tecnológicas), 28040 Madrid, Spain; natalia.brea@ciemat.es
3 Energy Department, CIEMAT (Centro de Investigaciones Energéticas, Medioambientales y Tecnológicas), 28040 Madrid, Spain; laura.bonales@ciemat.es
4 Institute of Optoelectronic Systems and Microtechnology, Polytechnic University of Madrid, 28040 Madrid, Spain; andres.velasco@upm.es (A.V.); javier.martinez@upm.es (J.M.)
5 Department of Electronic Engineering, E.T.S.I de Telecomunicación, Polytechnic University of Madrid, 28040 Madrid, Spain
6 Department of de Materials Science, E.T.S.I de Caminos, Canales y Puertos, Polytechnic University of Madrid, 28040 Madrid, Spain
* Correspondence: hanna.bukovska@ciemat.es (H.B.); mariabelen.gomez@ciemat.es (M.B.G.-M.); Tel.: +34-913466546 (H.B. & M.B.G.-M.)

Abstract: Many of the graphene-based structures exhibit an adsorption capacity due to their high specific surface area (SSA) and micropore volume. This capacity makes them competent materials for applications in energy and environmental sectors where efficiency is highly dependent on these properties for applications, such as water decontamination, solar cells or energy storage. The aim of this work is to study graphene-related materials (GRM) for applications where a high SSA is a requirement, considering the ideal SSA of graphene ≅ 2600 m^2g^{-1}. For the synthesis of most of the GRMs, some oxidation method such as the Tour method is used to oxidize graphite to graphite oxide (GrO) as an initial step. Our work studies the optimization of this initial step to evaluate the best conditions to obtain GrO with the maximum possible SSA. The different parameters influencing the process have been evaluated and optimized by applying an experimental design (ED). The resulting materials have been characterized by Brunauer–Emmett–Teller (BET), elemental analysis (EA), X-ray diffraction (XRD) and Raman and scanning electron microscopy (SEM). The evaluation of the results shows a maximum SSA of GrO of 67.04 m^2g^{-1} for a temperature of 60 °C, a time of 12 h, a H_2O_2 volume of 50 mL and 4 g of $KMnO_4$.

Keywords: Tour method; experimental design; graphite oxide; optimization; specific surface area

check for updates

Citation: Bukovska, H.; García-Perez, F.; Brea Núñez, N.; Bonales, L.J.; Velasco, A.; Clavero, M.Á.; Martínez, J.; Quejido, A.J.; Rucandio, I.; Gómez-Mancebo, M.B. Evaluation and Optimization of Tour Method for Synthesis of Graphite Oxide with High Specific Surface Area. *C* **2023**, *9*, 65. https://doi.org/10.3390/c9030065

Academic Editors: Jorge Bedia and Carolina Belver

Received: 31 May 2023
Revised: 23 June 2023
Accepted: 26 June 2023
Published: 5 July 2023

1. Introduction

Many of the latest energy and environmental needs require the use of materials with very specific properties, such as low thermal resistance, high electrical conductivity, high specific surface area, porosity or light weight, to meet their goals. Materials with high specific surface area (SSA) are particularly requested, as the efficiency of many industrial applications of importance, such as solar panels manufacturing, batteries or supercapacitors, depends on this very property. Over the last decades, the use of advanced high-SSA materials has highly increased: e.g., metal–organic frameworks [1–3], graphitic carbon nitrides [4,5], graphene oxide-based nanomaterials [6,7], zeolites [8–10] or porous metal

oxides [11,12], use in catalysis due to their adsorption capacity [13–16], hydrogen storage [17,18], water decontamination [19–22] or removal of radioactive elements [23,24]. For all these applications, graphene stands out as a material with an exceptionally high SSA, 2600 m^2g^{-1} [25]. Graphene is defined as a two-dimensional one-atom-thick material, consisting of a hexagonal lattice of carbon atoms [26]. Since it was first obtained in 2004 [27], it has increasingly attracted the interest of many researchers for bringing together a number of properties that are difficult to combine in a single material, such as transparency [28], strength [29], electrical conductivity [30], flexibility [31] and biocompatibility [30,32,33]. Those properties make graphene a highly versatile material for a wide range of applications: sensors [34], drug delivery [35], anti-corrosion coatings [36], solar panels [37] or electronics [28,31,38]. However, production issues, such as high energy consumption, pollution or the requirement for expensive equipment, direct band gas or the need for functionalization, mean that for most applications of graphene, its use as a pure material is not feasible. For this reason, work is usually carried out with materials derived from graphene, which are able to maintain most or some of the properties of interest of graphene, depending on the specific goals and applications pursued. GRM can be obtained in the form of fibers [39–41], films [42–44] or three-dimensional structures [16,45–47]. They also have the advantage that they can be doped or functionalized with different elements or compounds to improve them and therefore make them more suitable for each application [48–53]. One graphene material that stands out for its high SSA is the graphene aerogel (GA), which also has a low density and high porosity.

In most GA synthesis methods, graphene oxide (GO) is used as the starting material [54–57]. It is also the starting material for other graphene-related materials such as reduced graphene oxide (rGO), which is also able to reach high values of SSA [58]. In addition, GO in its initial form can be used in a multitude of applications, e.g., for microwave absorption [59,60]. The presence of oxygenated functional groups on the surface of graphene sheets gives them great versatility to carry out different chemical syntheses, i.e., joining them to form aerogel [54,55,61–63], reducing them into rGO [64–66] or functionalizing them with different organic and inorganic compounds [67,68]. Additionally, GO has a soluble structure in polar media like water, which is used as a solvent for many syntheses methods of this type [69–71].

In order to obtain GO, graphite is initially oxidized to graphite oxide (GrO), thus increasing the initial distance between the graphite sheets by introducing oxygenated functional groups that eliminate some of the double bonds of the graphene layers. This decreases the pi interactions between graphite sheets. Therefore, the process of oxidation of graphite to GrO is the initial step in most GRM synthesis methods and will determine both the degree of oxidation and the SSA of the GrO obtained. The first study on the oxidation of graphite was described by Brodie in 1859 [72], where $KClO_3$ and nitric acid were used to treat a suspension of graphite for 4 days at 60 °C. Subsequent studies focused on improving the efficiency of the process and decreasing the risk of explosion due to $KClO_3$. Staudenmaier replaced HNO_3 by a mixture of HNO_3 and H_2SO_4, improving the efficiency of the process [73], which could thus be carried out in a single step. However, this method did not avoid the risk of explosion because it still used $KClO_3$ and high temperatures. In 1958, Hummers and Offeman developed a new, faster, more efficient and safer method [74], in which the graphite was treated with $NaNO_3$, H_2SO_4 and $KMnO_4$. Although it is currently one of the most widely used and modified methods, one of the disadvantages is the generation of toxic gases (NO_2 and N_2O_4) from $NaNO_3$. This problem is avoided with the Marcano–Tour method [75,76], in which the use of $NaNO_3$ is eliminated and the oxidation process is carried out with a mixture of H_2SO_4 and H_3PO_4 (9:1) and larger amounts of $KMnO_4$.

The aim of this work is to optimize the process of graphite oxidation. A thorough study of this step is necessary to be able to control and evaluate the SSA, degree of oxidation and porosity of the starting GrO obtained for the synthesis of different GRM. Obtaining a GrO with a high SSA is conclusive for subsequently obtaining GRM materials with

a high SSA, which has a direct influence on many applications. For this purpose, the Tour method has been employed, since this method achieves higher degrees of oxidation and does not produce toxic gases [77] (compared to the Hummers method [78]). An experimental design (ED) has been developed with the main parameters that affect the synthesis of the method. These parameters are temperature, time and certain quantities of reagents. The SSA, percentage of carbon (% C) and t-Plot micropore volume (MV) have been chosen as responses of ED since they are the characteristics that have a conclusive role in most adsorption-related applications. In general, studies of the influence of the different process variables are carried out individually, leaving the rest of the variables fixed. This methodology has the disadvantage that the interactions between variables cannot be taken into account, therefore losing part of this information. In our work, a study of all the major variables that can influence the GrO synthesis process is addressed simultaneously, giving rise to a thorough analysis of both the effect of each individual variable and the interactions that appear among them, as well as the properties of the materials obtained under different experimental conditions. With good knowledge of how the different parameters affect the material obtained, a starting point is set for the regulation of its properties and structure according to the needs of future studies and applications.

The extensive characterization carried out on all the GrO samples has provided additional information on the most influential variables in the synthesis, as well as allowing us to verify the method used in the ED.

2. Materials and Methods

2.1. Materials

Graphite powder (<200 μm, synthetic) was purchased from Sigma Aldrich (Riedstr. Steinheim, Switzerland). Phosphoric acid (H_3PO_4, 85% w/w), concentrated sulfuric acid (H_2SO_4, 98% w/w), potassium permanganate ($KMnO_4$) and hydrogen peroxide (H_2O_2, 33% v/v) were of analytical grade from Merck (Darmstadt, Germany); hydrochloric acid (HCl, 37% w/w) was from GlobalChem (Cosela S.L., Seville, Spain); and ultrapure water (Resistivity $\geq$18.2 MΩ·cm^1) was from Milli-Q system (Millipore Bedford, Bedford, MA, USA).

2.2. Synthesis of Graphite Oxide Based on the Tour Method

For the synthesis of graphite oxide, the Tour method [75,76,79,80] has been employed. For this purpose, 300 mL of a mixture of H_2SO_4 and H_3PO_4 (9:1 v/v) was prepared to which 0.5 g of graphite was added with stirring. Then, $KMnO_4$ (3 or 4 g) was added slowly, at a time range of 30 min. The mixture was left stirring (for 12 or 16 h) at a certain temperature (45 or 60 °C). After this time, 250 mL of distilled water cooled in ice is added drop by drop. This process lasts about 30 min. Finally, H_2O_2 (10 or 50 mL) was added, generating a light-yellow mixture. The reaction mixture was allowed to settle overnight. The next day the supernatant liquid was removed with a pipette and the solid was washed twice with 150 mL of a 10% HCl solution. The obtained graphite oxide was centrifuged for 1 h at 8000 rpm, diluting it in water up to 350 mL. This process was repeated until the centrifugation liquid reached a pH of 5–6. Then, the product was placed in Petri dishes, frozen for 48 h and freeze-dried for 5 days. Figure 1a shows an example of a Petri dish with GrO after freeze-drying, while Figure 1b shows the lamellar structure formed in the material after this process. Finally, the material obtained is ground with a ball mill (Retsch (Haan, Germany), MM400) at 7 Hz for 6 min.

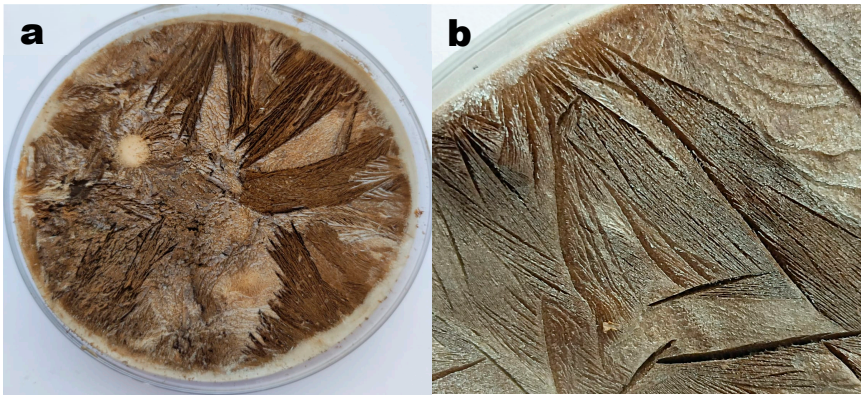

Figure 1. (**a**) GrO after freeze-drying; (**b**) lamellar structure formed in GrO after freeze drying.

2.3. Experimental Design

A screening ED (factorial design with two levels and four factors, 2^4) was carried out using STATGRAPHICS Centurion XVII. SSA, percentage carbon (% C) and t-Plot MV were chosen as study responses. The experimental factors used were temperature, time, weight of $KMnO_4$ and volume of H_2O_2. For each experimental factor, two values have been defined—for temperature, 45 and 60 °C; for time, 12 and 16 h; for $KMnO_4$, 3 and 4 g; and for H_2O_2, 10 and 50 mL—thus establishing the 16 experiments shown in Table 1.

Table 1. Experimental conditions of the 16 experiments obtained with the ED.

Experiment	Temperature (°C)	Time (h)	H_2O_2 (mL)	$KMnO_4$ (g)
GrO_Exp01	60	12	50	4
GrO_Exp02	45	16	50	3
GrO_Exp03	45	12	10	4
GrO_Exp04	45	12	10	3
GrO_Exp05	45	12	50	4
GrO_Exp06	45	16	10	4
GrO_Exp07	60	16	10	4
GrO_Exp08	45	16	50	4
GrO_Exp09	60	16	10	3
GrO_Exp10	60	12	50	3
GrO_Exp11	60	16	50	4
GrO_Exp12	45	16	10	3
GrO_Exp13	60	12	10	3
GrO_Exp14	60	16	50	3
GrO_Exp15	45	12	50	3
GrO_Exp16	60	12	10	4

2.4. Characterization

To evaluate structural parameters and how they influence adsorption process—in particular, the interaction potential between the pore surface and gas—N_2 adsorption/desorption processes were applied at 77 K temperature, employing ASAP 2020 (Micromeritics, Norcross, GA, USA) equipment. The Brunauer–Emmett–Teller (BET) method was applied to determine the specific surface area (SSA). At the same time, the morphology of the pores plays an important role, so the micropore volume was evaluated using the t-plot method.

The total carbon content was determined by combustion using a TruSpec CHN elemental analyzer (LECO, Benton Harbor, MI, USA). This method determines the carbon content by heating to a temperature of at least 900 °C in the presence of oxygen gas. Then, graphene was oxidized and/or volatilized to carbon dioxide (CO_2). The amount of carbon dioxide was measured using an infrared detection method.

Structural studies were performed employing X-ray diffraction (XRD) equipment, X'Pert Pro diffractometer (Malvern PANalytical, Malvern, UK), with Cu K_ radiation (λ = 1.54 Å) with an operating at 45 kV and 40 mA. XRD data were collected in θ–θ configuration in the angular range of 5 < 2 < 80 with a 0.017 step size.

Raman spectra were acquired using a B&WTek i-RamanTM, ExemplarPro model, with an operation power of 100 mW. A green HeNe laser with a wavelength of 532 nm was focused onto the sample. The scattered radiation was then collected obtaining a resolution of 2.99 cm^{-1}/pixel.

The morphology of the samples was observed using scanning electron microscopy (SEM), using a FEI InspectTM F50 (FEI Company, Columbia, MD, USA) at 5 kV of accelerating voltage. Some images were taking of each sample to the same different magnifications in order to compare the images.

3. Results and Discussion

3.1. Experimental Design Analysis

The experimental design has been completed with the introduction of the results obtained for % C, SSA and t-Plot MV as responses in the software: STATGRAPHICS Centurion XVII. The importance and influence of the different variables of the synthesis process on these responses has been analyzed. For this purpose, standardized Pareto diagrams and main effects plots have been represented for each response (Figures 2–4). The Pareto diagrams (Figures 2a, 3a and 4a) show horizontal bars representing the value of the T-Statistic of the effects of each variable and interaction of variables on the studied responses. These bars are ordered from highest to lowest according to the level of significance. Grey bars indicate that the effect of the variable on the studied response is positive, while blue bars indicate a negative effect. Bars above the vertical blue line are considered statistically significant at a 5% confidence level. On the other hand, the main effects plots (Figures 2b, 3b and 4b) represent the estimated variation for the responses as a function of the different process variables. This estimation is plotted when each variable moves from its lowest value to its highest value with the rest of the variables set at an intermediate value between the two levels.

Figures 2 and 3 show the standardized Pareto diagrams and main effects plots for SSA and t-Plot MV, respectively. The Pareto diagrams (Figures 2a and 3a) show that the variable with the strongest influence on both responses is temperature, which is statistically significant, especially in the case of t-Plot MV. In the main effect plots (Figures 2b and 3b), a similar variation can be seen for both SSA and t-Plot MV with respect to the different variables. Both responses increase with increasing temperature and increasing amounts of $KMnO_4$ and H_2O_2 and decrease with time.

During the graphite oxidation process, CO_2 bubbles are generated at around 45 °C and above, as described in the literature [81]. As the temperature increases, both the oxidation process and the CO_2 generation rate or extension can be higher, leading to a greater separation of the GO sheets with an exfoliation effect. In addition, at 55 °C and above, thermal decomposition of the intermediate species Mn_2O_7 occurs [82], producing O_2 bubbles, which contributes to the exfoliation process. Residual $KMnO_4$ causes the same effect by introducing oxygenated groups in the basal planes that separate the graphite sheets from each other [83,84]. H_2O_2 contributes to increasing the degree of exfoliation-generating O_2^{2-} that intercalates between the graphite sheets [80,85]. Time has a negative effect on both responses due to the effect of over-oxidation [86–88], since greater amounts of oxygenated functional groups are formed at longer times. This results in the fragmentation and degradation of the GrO structure.

Figure 4 shows the Pareto diagram and main effects diagram for % C. The Pareto diagram (Figure 4a) shows that the factor that most influences this response is the interaction between H_2O_2 volume and temperature. This interaction has a positive effect on % C, although it is not statistically significant. This interaction has the most positive influence on the SSA and t-Plot MV graphs also, although in both cases, it is not statistically significant. It could be assumed from the data collected that the most influential variables are temperature and time.

The main effects plot (Figure 4b) shows that the % C decreases with increasing temperature, time and amount of H_2O_2 and increases with increasing amount of $KMnO_4$. As the temperature increases, the oxidation rate of the graphite increases [75], resulting in a more oxidized GrO product with a lower carbon content. With increasing time, more oxygenated groups are incorporated [84], generating the same effect. It is likely that the addition of more H_2O_2 produces the exfoliation effect mentioned above, opening and exposing intact areas of GrO sheet to the oxidant. This effect could cause a larger surface area of GrO to be oxidized, consequently decreasing the carbon ratio. $KMnO_4$ contributes to increasing the percentage of C due to the effect of over-oxidation [88].

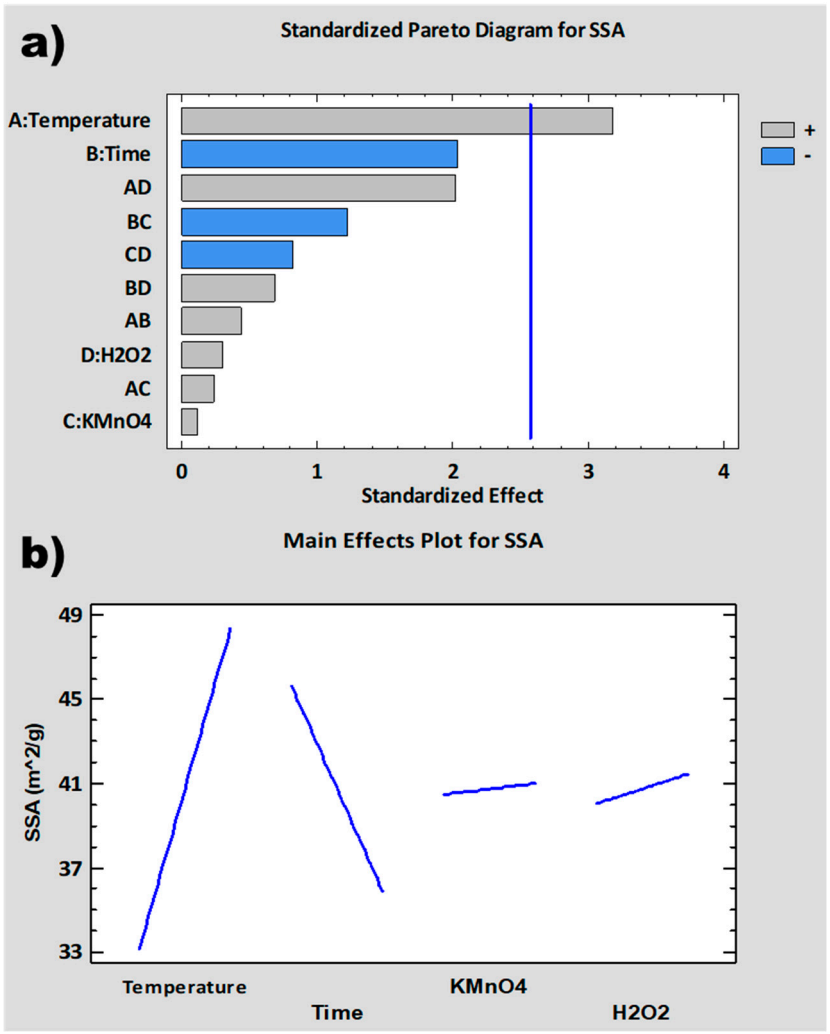

Figure 2. SSA analysis: (**a**) normalized Pareto diagram; (**b**) main effect plot.

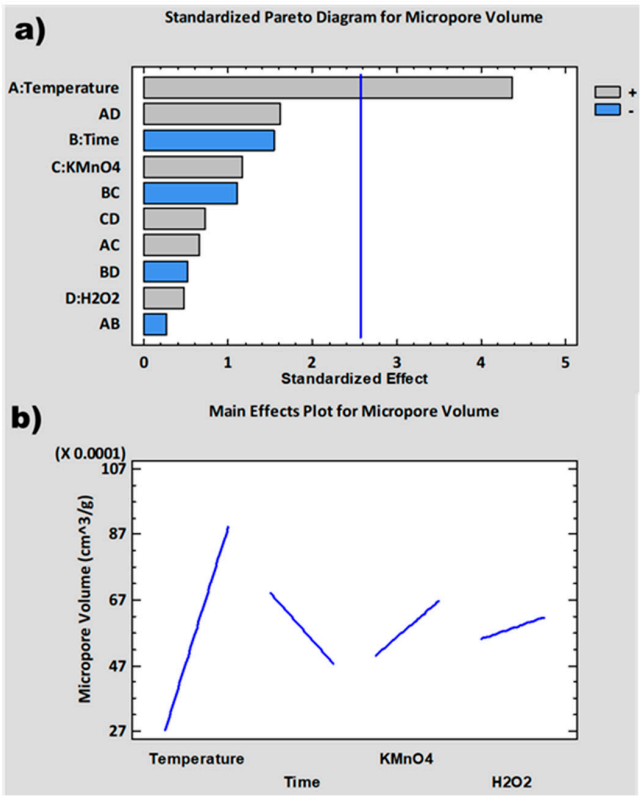

Figure 3. Micropore volume analysis: (**a**) normalized Pareto diagram; (**b**) main effect plot.

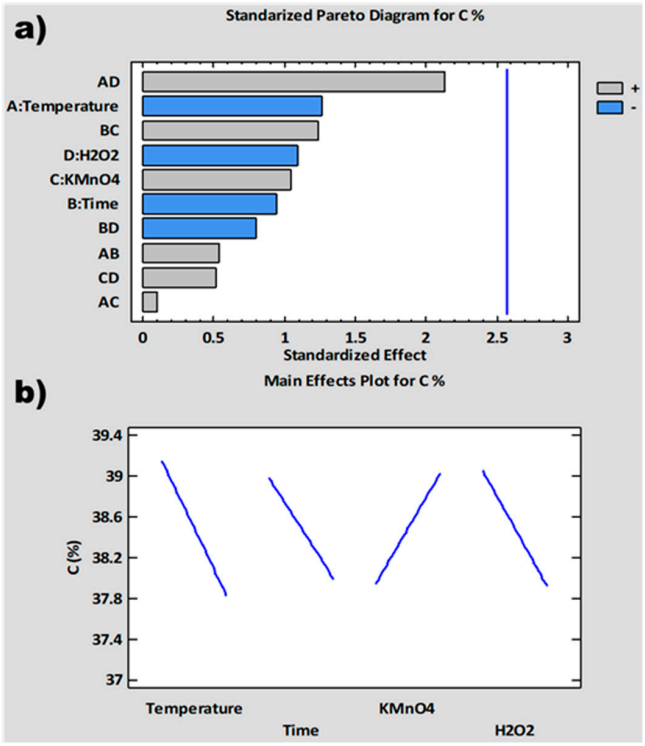

Figure 4. % C analysis: (**a**) normalized Pareto diagram; (**b**) main effect plot.

Finally, according to the ED performed, the synthesis conditions with the best conditions for the oxidation of graphite to GrO are shown in Table 2.

Table 2. Optimum synthesis conditions obtained by applying ED.

Variable (units)	Optimum Value
Temperature (°C)	60
Time (h)	12
H_2O_2 (mL)	50
$KMnO_4$ (g)	4

The best experimental conditions correspond to GrO_Exp01 of the ED, where an SSA of 67.04 m^2g^{-1}, a t-Plot MV of 0.018 cm^3/g and a % C of 38.9 are obtained. After examining the results obtained in the ED, a clear difference between the GrO samples obtained at 45 °C and those at 60 °C is observed. The latter seem to be more affected by the processes of CO_2 release and Mn_2O_7 decomposition, which generate an additional exfoliation in the materials. According to the Pareto diagrams obtained in the ED, temperature is the most influential factor in the graphite oxidation process.

3.2. Sample Characterization

In addition to the ED, all samples have been characterized chemically, structurally and morphologically. The relevant parameters have been calculated for each of the applied techniques and the influence of each of the process variables has been evaluated individually by calculating the T-student (5% confidence, reference value: 1.89) for each response. In this way, the influence of the variables on the parameters calculated for each technique can be established.

3.2.1. BET Analysis

The different GrO samples obtained were analyzed by BET, using the N_2 adsorption and desorption method to determine the SSA and t-Plot MV. Table 3 shows the range, average, SD and T-Student of the results corresponding to SSA and t-Plot MV. The full results can be found in Table A1, in Appendix A.

The SSA data show an overall range of 23.4–67.0 (m^2g^{-1}). The maximum value obtained is higher than those obtained by other authors using the same synthesis [89]. It is remarkable that the maximum value comes out at the shortest time.

The highest SSA average values have been obtained in the samples synthesized at 60 °C, 12 h, 50 mL H_2O_2 and 4 g $KMnO_4$. Considering the calculation of the T-Student, it can be seen that the results obtained in the temperature variation are statistically discrepant. However, variations in the amounts of H_2O_2 and $KMnO_4$ do not produce significant changes in the SSA of the obtained GrO.

In the case of t-Plot MV data, the overall range is between 0.0009–0.0181 (cm^3g^{-1}). The difference in the obtained results is of two orders of magnitude.

The average values of t-Plot MV show a similar variation to those obtained for SSA, the samples synthesized at 60 °C, 12 h, 50 mL H_2O_2 and 4 g $KMnO_4$ being the ones with the highest t-Plot MV. According to the results obtained from T-Student, a significant discrepancy between the results obtained with the maximum and minimum temperature values is observed, as in the case of SSA, while variations in time and amounts of H_2O_2 and $KMnO_4$ do not produce significant changes.

These results are in agreement with those obtained by ED, where the Pareto diagrams show that the variable that most affects SSA and t-Plot MV is temperature, and in this case, the results are also statistically discrepant.

Considering that most environmental and energy applications based on adsorption require high SSA and porosity, the best synthesis conditions would be at higher temperatures and reagent quantities and short times.

Table 3. Range, average, SD and T-Student of the results corresponding to SSA and t-Plot MV of the 16 GrO samples obtained in the ED.

Variable	Value	SSA (m^2g^{-1})			
		Range	Average	SD	T-Student
T (°C)	45	23.4–57.4	33.2	11.6	3.0
	60	40.6–67.0	48.3	8.9	
t (h)	12	25.1–67.0	45.6	13.6	1.6
	16	23.4–51.2	35.9	10.3	
H_2O_2 (mL)	10	25.3–57.4	40.0	10.5	0.22
	50	23.4–67.0	41.5	15.2	
$KMnO_4$ (g)	3	25.3–51.2	40.5	9.4	0.05
	4	23.4–67.0	41.0	15.9	
Variable	**Value**	**t-Plot-(Micropore Volume, cm^3g^{-1})**			
		Range	**Average**	**SD**	**T-Student**
T (°C)	45	0.0009–0.0059	0.0028	0.0015	4.4
	60	0.0070–0.0181	0.0089	0.0037	
t (h)	12	0.0022–0.0181	0.0069	0.0050	1.0
	16	0.0009–0.0082	0.0048	0.0031	
H_2O_2 (mL)	10	0.0021–0.0080	0.0055	0.0024	0.31
	50	0.0009–0.0181	0.0062	0.0057	
$KMnO_4$ (g)	3	0.0009–0.0082	0.0050	0.0030	0.01
	4	0.0021–0.0181	0.0067	0.0052	

3.2.2. Elemental Analysis

All the samples obtained were analyzed to determine their total C content. Table 4 shows the range, average, SD and T-Student of the results corresponding to carbon percentage.

Table 4. Range, average, SD and T-Student of the results corresponding to C content of the 16 GrO samples obtained in the ED.

Variable	Value	C (%)			
		Range	Average	SD	T-Student
T (°C)	45	34.6–43.1	39.1	2.8	1.2
	60	35.4–39.0	37.8	1.1	
t (h)	12	37.6–42.4	39.0	1.7	0.88
	16	34.6–43.1	38.0	2.7	
H_2O_2 (mL)	10	35.4–43.1	39.1	2.5	1.0
	50	34.6–40.5	37.9	1.8	
$KMnO_4$ (g)	3	34.6–42.4	38.0	2.4	0.12
	4	36.5–43.1	39.0	2.0	

The carbon percentage data show an overall range of 34.6–43.1 (%). The samples synthesized at a temperature of 45 °C present a slightly higher C content (average carbon content of 39.1%) than those synthesized at 60 °C (average: 37.8%). The highest % C average values were obtained in samples synthesized at 45 °C, 12 h, 10 mL H_2O_2 and 4 g $KMnO_4$. It is observed that none of the values obtained for T-Student exceed the critical value, indicating that variations in temperature, time and amounts of H_2O_2 and $KMnO_4$ do not produce significant changes in the % C of the GrO obtained.

These results are in agreement with those obtained by ED, where the Pareto diagrams (Figure 4a) show that none of the experimental variables are statistically significant with respect to the % C values. The full results can be found in Table A2 in Appendix A.

In this case, the optimum % C depends on the intended application. GrO with lower % C could subsequently undergo different reduction treatments to recover the initial graphitic structure of the sheets and be used in applications requiring electrical conductivity, while more oxidized GrO are very versatile; thus, they can be chemically functionalized to improve their properties for selective adsorption applications.

3.2.3. XRD Analysis

The different GrO samples obtained after carrying out the 16 experiments of the ED have been analyzed by XRD to determine structural parameters. The XRD pattern of pure graphite presents a peak at $2\theta = 26.58°$ (2θ) corresponding to the [002] diffraction plane and an interplanar distance, d = 0.335 nm [90]. In the oxidation process, the [002] diffraction plane broadens and decreases in intensity, while the [001] diffraction plane of GrO, appears at $2\theta = 11°$ [91]. This variation is due to the introduction of oxygenated groups, mainly hydroxy and epoxy on the surface of the individual graphene sheets, and carboxyl groups on the edges that break the crystalline structure. The presence of oxygenated groups increases the interplanar distance, distorting the initial structure of the stacked sheets. Figure 5 shows the [001] diffraction plane corresponding to the GrO materials synthesized in the 16 experiments. The diffraction maxima of all GrO come out in the range of $9.83° < 2\theta < 11.77°$, corroborating that oxidation of graphite to GrO has occurred.

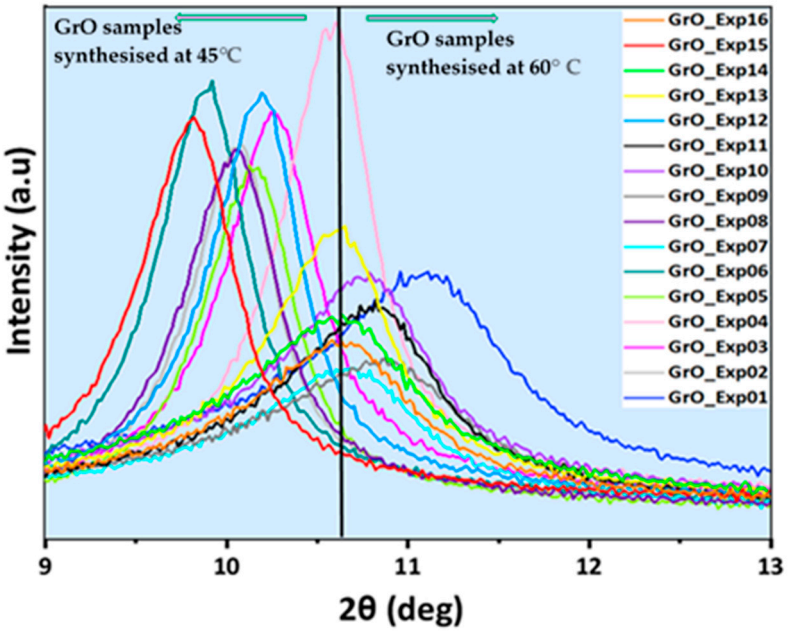

Figure 5. Graph of [001] diffraction peak for the 16 GrO samples obtained in ED.

It can be seen that there is a clear difference between the samples synthesized at the two temperatures (the vertical black line marks an arbitrary division between the diffractograms of GrO synthesized at 45 °C and at 60 °C). The diffraction peaks corresponding to GrO synthetized at 45 °C (GrO_Exp02-06, 08, 12 and 15) are narrower and more intense, while those synthesized at 60 °C (GrO_01, GrO_07, GrO_09-11, GrO_13, GrO_14, GrO_16) are less intense and wider. This could be due to the fact that at 45 °C, in this type of materials, gaseous CO_2 can start to be produced [81], which could be adsorbed between the GrO films, and it can be desorbed and leave the material if there is high enough energy [92], producing a certain degree of exfoliation and defects in the films, as mentioned previously in Section 3.1. On the other hand, according to the literature, Mn_2O_7 decomposes at 55 °C

and above [82], generating bubbles and facilitating the separation of the GrO sheets. GrO samples synthesized at 60 °C are more affected by these phenomena, which produce distortion in the stacked structure, generate defects in the films, decrease crystallinity and cause exfoliation, giving rise to wider diffraction peaks of lower intensity. Additionally, the samples obtained at 45 °C show narrower and more intense diffraction peaks as they retain a greater proportion of stacked structure; therefore, the crystallinity of GrO is higher. This can be due to the fact that during their synthesis processes, they have been kept at the temperature at which CO_2 bubbles start to form, and most of them do not have enough energy to leave the material. These results are in agreement with those obtained in the ED, where the temperature is the most relevant parameter and statistically significant for SSA and t-Plot MV.

The average, SD and T-Student of the results corresponding to the 2θ positions, interplanar spacing (d), number of stacked layers (n) and crystal size (L) of the GrO obtained have been summarized in Table 5 (the full results can be found in Table A3 in Appendix A). The number of stacked layers in the graphite oxide (n) was obtained by Equation (1), where "L" is the crystal size and "d" is the interplanar spacing:

$$n = \frac{L}{d} \quad (1)$$

Furthermore, L has been calculated using the Scherrer Equation (2) [93]:

$$L = (0.94 \times \lambda)/(\beta \times \cos\theta), \quad (2)$$

where λ is the X-ray wavelength, β is the line broadening at half the maximum and θ is the Bragg angle.

In Table 5a, the average position and d data show an overall range of 9.8–11.2 (2θ) and 0.79–0.90 (nm), respectively. It can be observed that the average values for position only show variations in the case of temperature changes, being statistically significant according to the obtained T-Student value (7.7). The same trend can be seen for d, for which a T-Student value of 7.5 has been calculated, exceeding the critical value only in the case of variations in the synthesis temperature.

On the other hand, Table 5b shows the calculated values of n and L according to the formulae mentioned above (Equations (1) and (2)). The ranges of total average values for n and L are 27.7–166.1 (nm) and 33.7–197.7, respectively. For both cases, the T-Student exceeds the critical value only in the case of temperature variations, reaching a value of 4.5 in the case of L and 4.3 for n.

The general goal is to obtain more porous structures with higher SSA and GrO with smaller crystal sizes and a lower number of stacked layers. In this case, the best conditions are reached working at higher temperatures, since at 60 °C, an average L and n of 38.5 and 47.3 nm, respectively, are obtained, compared to 109.3 and 125.4 nm obtained at 45 °C.

According to Table 5a,b, the GrO synthesized at 60 °C has a smaller average interplanar distance (0.81 nm) and a smaller average number of stacked layers [47] compared to those synthesized at 45 °C (0.87 nm and 125), although the interplanar distance differences are slight.

This could be due, in part, to a slight accumulation of CO_2 bubbles, which starts to form at 45 °C, as described in previous sections. At this temperature, the gas bubbles do not yet have enough energy to leave the GrO structure, so they could be adsorbed between the sheets, generating pressure and increasing the interplanar spacing. On the other hand, at 60 °C, the CO_2 generation is higher, together with a higher oxidation of the graphite. At this temperature (60 °C), the CO_2 bubbles formed have enough energy to leave the GrO structure, which could result in smaller interplanar spacings than in the samples synthesized at 45 °C. However, the interplanar spacing in GrO depends on multiple factors in addition to this, such as the water content [94,95] and the number of stacked layers [96], among others. Moreover, most of these factors are influenced by each other, such as CO_2

adsorption, which depends on the degree of hydration [97], which, in turn, depends on the number of stacked layers [96].

Table 5. Range, average, SD and T-Student of the results of the 16 GrO samples obtained in the ED corresponding to (a) position (2θ) and d (nm); (b) L (nm) and n.

(a)					
Variable	**Value**	**Position (2θ)**			
		Range	**Average**	**SD**	**T-Student**
T (°C)	45	9.8–10.5	10.1	0.22	7.7
	60	10.6–11.2	10.9	0.15	
t (h)	12	9.8–11.2	10.5	0.42	0.34
	16	9.9–10.9	10.5	0.44	
H_2O_2 (mL)	10	9.9–10.9	10.5	0.36	0.14
	50	9.8–11.2	10.5	0.49	
$KMnO_4$ (g)	3	9.8–10.9	10.5	0.40	0.0082
	4	9.9–11.2	10.5	0.46	
Variable	**Value**	**d (nm)**			
		Range	**Average**	**SD**	**T-Student**
T (°C)	45	0.84–0.90	0.87	0.019	7.5
	60	0.79–0.83	0.81	0.011	
t (h)	12	0.79–0.90	0.84	0.034	0.34
	16	0.81–0.89	0.85	0.035	
H_2O_2 (mL)	10	0.81–0.89	0.84	0.029	0.18
	50	0.79–0.90	0.85	0.040	
$KMnO_4$ (g)	3	0.81–0.90	0.85	0.033	0.16
	4	0.79–0.89	0.84	0.036	
(b)					
Variable	**Value**	**L (nm)**			
		Range	**Average**	**SD**	**T-Student**
T (°C)	45	58.6–166.1	109.3	43.4	4.5
	60	27.7–49.8	38.5	7.5	
t (h)	12	33.2–166.1	74.8	49.8	0.073
	16	27.7–166.1	73.0	48.2	
H_2O_2 (mL)	10	35.6–166.1	80.4	54.2	0.54
	50	27.7–124.6	67.4	42.1	
$KMnO_4$ (g)	3	27.7–166.1	82.7	59.8	1.8
	4	35.6–124.6	65.2	32.6	
Variable	**Value**	**n**			
		Range	**Average**	**SD**	**T-Student**
T (°C)	45	67.0–197.7	125.4	50.9	4.3
	60	33.7–61.6	47.3	9.2	
t (h)	12	40.8–197.7	87.8	57.1	0.10
	16	33.7–189.9	84.9	53.8	
H_2O_2 (mL)	10	42.8–197.7	94.6	62.5	0.60
	50	33.7–141.7	78.1	45.9	
$KMnO_4$ (g)	3	33.7–197.7	96.5	68.4	1.8
	4	43.8–141.7	76.2	35.4	

The increased production of CO_2 bubbles at higher temperatures also generates a higher degree of exfoliation and fragmentation in the materials synthesized at 60 °C. These effects result in fewer stacked layers and smaller crystal size (38.5 nm) in GrO synthesized at 60 °C compared to those obtained at 45 °C (109.3 nm), which is in agreement with the SEM images described below in Section 3.2.5. This means that at higher temperatures, more graphitic surface area is exposed to the oxidant and oxidation occurs over a larger area. The higher degree of oxidation due to the exposure of more surface is corroborated by the results obtained by E.A, where lower % C are obtained for samples synthesized at 60 °C. Figure 6 shows the possible GrO structure synthesized at 45 and 60 °C, taking into account all the results obtained.

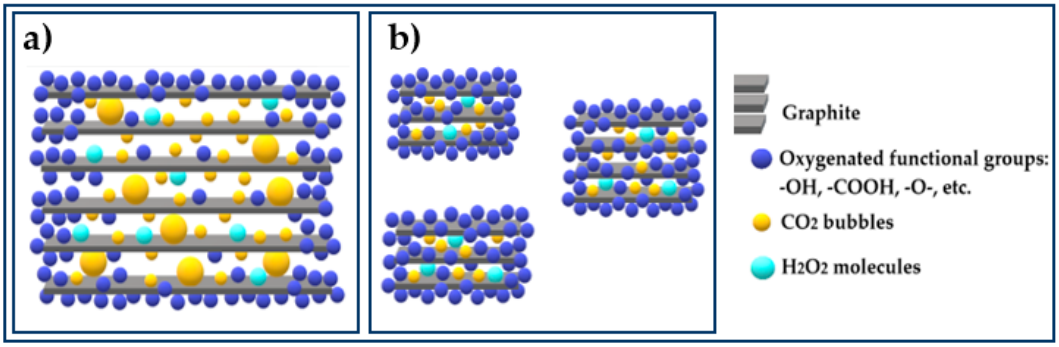

Figure 6. Schematic representation of GrO structures formed at: (**a**) 45 °C and (**b**) 60 °C.

3.2.4. Raman Analysis

In Raman spectroscopy, a typical spectrum corresponding to pure graphite presents three characteristic bands: G-band at ~1580 cm^{-1}, D-band at ~354 cm^{-1} and 2D-band at ~2700 cm^{-1} [98]. The G band is the most intense and is associated with the graphite mode [99]. It appears due to the first order dispersion of the E_2g_2 mode and is related to the number of sp^2 carbons. The D band is less intense and corresponds to the diamond mode. This band is attributed to disorder in the graphite, which may be due to amorphous carbon species, vacancies, defects in the structure, etc. [100]. The ratio of intensities of the D and G bands (I_D/I_G) is used to estimate the density of defects present in the material studied and has a value of approximately 0.23 in pure graphite. In the case of GrO, defects appear mainly after the oxidation process, which incorporates oxygenated groups, generating sp^3 carbons and distorting the graphitic structure. Therefore, by the graphite oxidation, the D band increases in intensity due to the creation of defects, the incorporation of heteroatoms in the interplanar space and the increase of domains with sp^3 carbons. On the other hand, the intensity of the G band decreases because the domains of sp^2 carbons become smaller, until it becomes comparable to the D band. In the case of GrO, the I_D/I_G ratio grows to ~1.0 due to the incorporation of defects and sp^3 carbons after the oxidation process. The 2D band is related to the number of stacked graphene layers within the graphitic structure. The I_{2D}/I_G ratio, which is inversely proportional to the number of stacked layers, is often used to evaluate it. Values in the range 2–3 correspond to monolayers, values <1 correspond to multilayers, while intermediate values are considered as bilayers [101].

The analysis of the 16 samples has provided the I_D/I_G ratios shown in Figure 7 in order from highest to lowest I_D/I_G ratio, read from the bottom to the top of the graph. Data were generated by measuring each sample at three different points and obtaining their average value. It is observed that all values are in the range $0.896 < I_D/I_G < 1.033$, indicating that defects and disorder have been generated in the structure during the oxidation process. There are no appreciable differences between the results of the samples synthesized at 45 °C and those obtained at 60 °C, but some influence of the amount of H_2O_2 is observed. Samples synthesized with 50 mL H_2O_2, such as GrO_Exp08, GrO_Exp05, GrO_Exp02, GrO_Exp11 and GrO_Exp14, show larger I_D/I_G values compared to others synthesized with 10 mL H_2O_2, such as GrO_Exp07, GrO_Exp04, GrO_Exp12, GrO_Exp03 and GrO_Exp16. This

may be due to the exfoliation effect of H_2O mentioned above, which generates disorder in the GrO structure and thus exposes larger graphitic surfaces to oxidation, leading to higher amounts of defects.

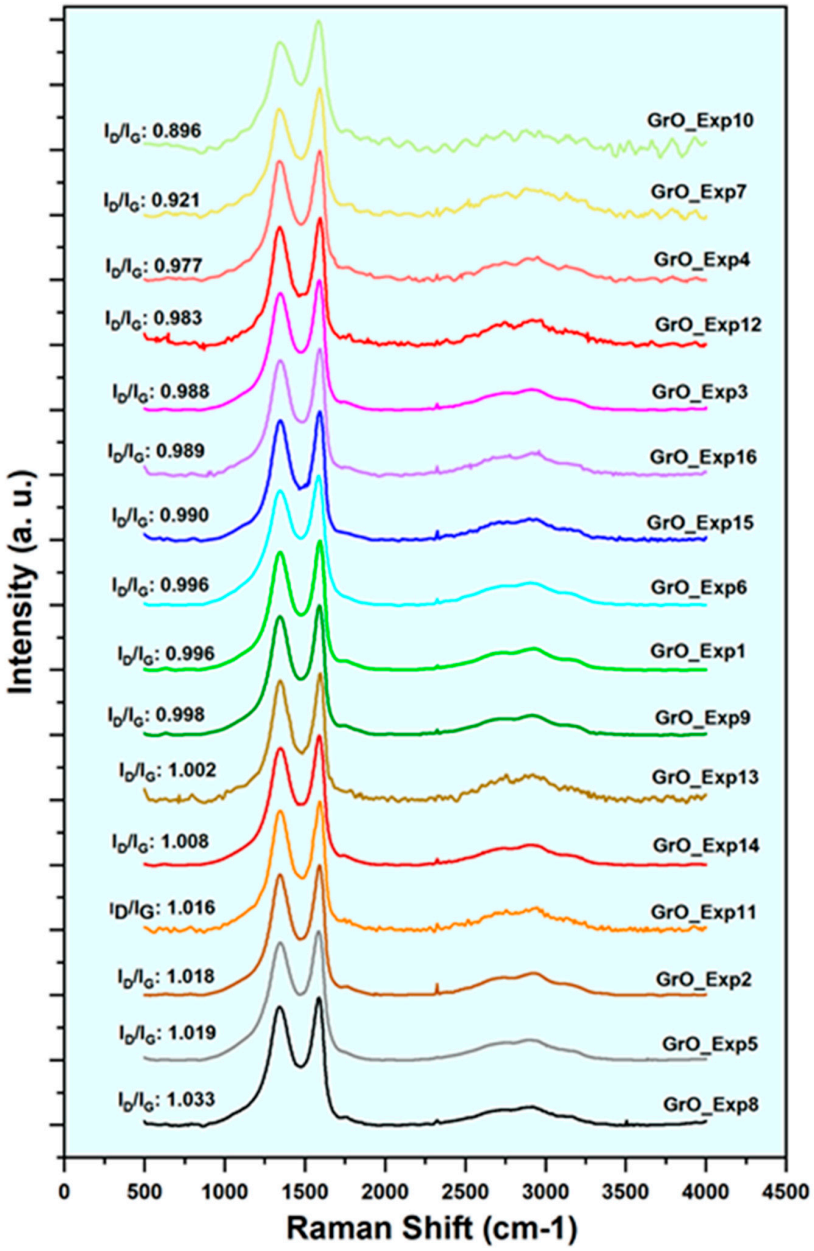

Figure 7. Raman spectra of the 16 GrO samples obtained in the ED, ordered from highest to lowest I_D/I_G ratio (from the bottom up).

Table 6 shows range, average, SD and T-Student of the results corresponding to the I_D/I_G and I_{2D}/I_G of the GrO obtained in the ED (the full results can be found in Table A4 in Appendix A). For I_D/I_G, a total range of average values of 0.90–1.03 can be observed. The highest T-Student is obtained for the case of temperature variations, with an I_D/I_G of 1.3; however, it does not exceed the critical value. On the other hand, the total range of average values for I_{2D}/I_G is between 0.13 and 0.18. According to the T-Student results, the variations of none of the studied variables are statistically significant for the I_D/I_G and I_{2D}/I_G ratios. The I_{2D}/I_G values obtained for both temperatures are very similar, indicating multilayer stacking in the GrO structure. This is in line with the XRD results discussed

in the previous section (Section 3.2.3), where the number of stacked layers are evaluated more accurately.

Table 6. Range, average, SD and T-Student of the results corresponding to I_D/I_G and I_{2D}/I_G content of the 16 GrO samples obtained in the ED.

Variable	Value	I_D/I_G			
		Range	Average	SD	T-Student
T (°C)	45	0.98–1.03	1.00	0.020	1.3
	60	0.90–1.02	0.98	0.044	
t (h)	12	0.90–1.02	0.98	0.037	0.80
	16	0.92–1.03	1.00	0.034	
H_2O_2 (mL)	10	0.92–1.00	0.98	0.026	0.86
	50	0.90–1.03	1.00	0.043	
$KMnO_4$ (g)	3	0.90–1.02	0.98	0.038	0.007
	4	0.92–1.03	1.00	0.034	
Variable	**Value**	I_{2D}/I_G			
		Range	**Average**	**SD**	**T-Student**
T (°C)	45	0.14–0.18	0.16	0.013	0.41
	60	0.13–0.17	0.15	0.012	
t (h)	12	0.13–0.16	0.15	0.011	0.66
	16	0.14–0.18	0.16	0.014	
H_2O_2 (mL)	10	0.14–0.18	0.16	0.012	0.70
	50	0.13–0.17	0.15	0.013	
$KMnO_4$ (g)	3	0.13–0.17	0.15	0.012	0.015
	4	0.14–0.18	0.16	0.012	

3.2.5. SEM Analysis

SEM analyses were also carried out to evaluate the morphology of the obtained GrO samples.

From the previous analysis, it can be reasoned that temperature is the most influential variable. Therefore, two samples have been selected (GrO_01 and GrO_05), in which the two different temperatures have been applied (45 and 60 °C), keeping the rest of the variables fixed (12 h, 50 mL H_2O_2 and 4 g $KMnO_4$) (Figure 8). It is in these two cases where the greatest morphological differences can be seen.

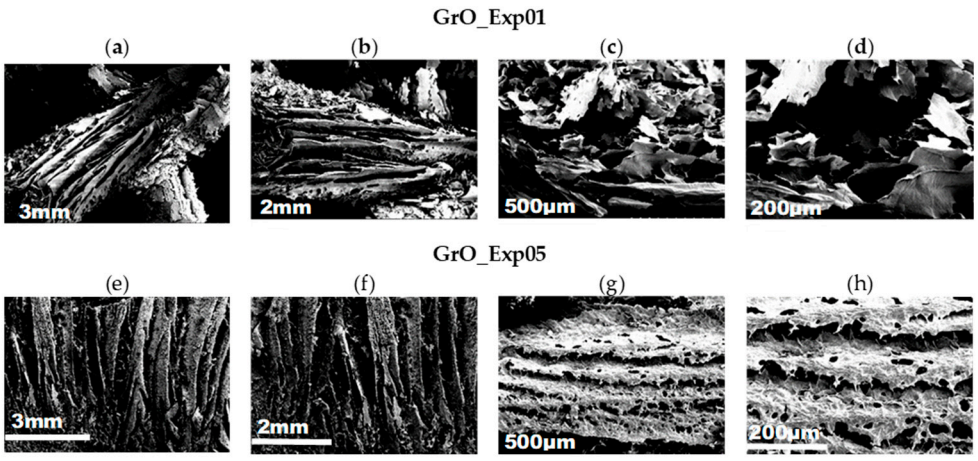

Figure 8. SEM images for GrO_Exp01 and GrO05 obtained at: (**a**,**e**) 15xmagnifications; (**b**,**f**) 20× magnifications; (**c**,**g**) 100× magnifications; (**d**,**h**) 200× magnifications.

In both samples, separate layers are observed, indicating partial exfoliation due to both the oxidation process and the freeze-drying process. The sample obtained at 60 °C (GrO_Exp01) shows a more disorganized structure and greater exfoliation, while in the sample obtained at 45 °C (GrO_Exp05), there are stacked layers with a certain degree of alignment, which is in agreement with the results obtained in XRD, where broader peaks were obtained at 60 °C. The most noticeable differences can be seen in Figure 8d,h corresponding to the two syntheses. In these cases, Figure 8d corresponding to the GrO_Exp01 synthesis, shows that the GrO sheets are smaller and more exfoliated and fragmented than in the GrO_Exp05 synthesis (Figure 8h), partly due to the formation of CO_2 bubbles which, in this case, are released and produce these effects. This observation corroborates the scheme made in Figure 6, which represents the possible structure of GrO obtained at the two temperatures studied thanks to the structural and morphological data provided by XRD Raman and SEM techniques.

4. Conclusions

The results of SSA, micropore volume and % C have been used as responses in the experimental design as variables of interest for specific applications. According to the Pareto diagrams, the variable that most influences the three responses is temperature, being statistically significant in the case of SSA and micropore volume. In the main effect plots, SSA and micropore volume vary similarly with changing experimental conditions. For both responses, an increase in temperature and the amounts of $KMnO_4$ and H_2O_2 positively influences the degree of exfoliation, which contributes to an increase in SSA and micropore volume, whereas syntheses at longer times result in GrO of lower SSA and micropores. On the other hand, % C decreases with increasing temperature, time, and amount of H_2O_2 and increases with increasing amount of $KMnO_4$. The optimal experiment, according to the experimental design, to maximize the three studied responses is the one corresponding to the following experimental conditions: temperature of 60 °C, H_2O_2 volume of 50 mL, $KMnO_4$ weight of 4 g and time of 12 h. These experimental conditions correspond to the GrO_Exp01 of the ED. However, it should be noted that the optimal conditions obtained depend on both the initial mass and the exact type of graphite used. Therefore, future work could consider extending the research by adding a study of the optimization with different graphite particle size distributions. However, we can conclude that temperature is the most relevant parameter in the Tour process.

The results of the T-Student values corroborate that temperature is the parameter that most statistically influences the SSA and t-Plot MV obtained. Furthermore, the calculation of this parameter has allowed us to determine that temperature is a parameter that also has a significant influence on the parameters calculated in XRD (2θ, d, L and n). Temperature is therefore the main parameter which influences most of the responses studied and whose control is the most decisive in regulating the properties of the materials obtained.

According to the XRD, Raman and SEM results, the structure of the GrO synthesized at 60 °C is less crystalline with more defects and shows a higher structural disorder than that of the GrO obtained at 45 °C. This may be due to a slight thermal exfoliation produced by the generation of CO_2 from 45 °C or the instability of Mn_2O_7 from 55 °C onwards. The generation of gaseous species that occur in both processes acts by separating and exfoliating the graphite layers. This is also corroborated by the results obtained in BET, according to which the SSA and micropore volumes are higher in samples obtained at 60 °C. In the elemental analysis results, it is observed that GrO samples synthesized at 45 °C have a higher % C compared to those synthesized at 60 °C, indicating lower oxygen content. This may be due to the higher exfoliation of GrO synthesized at 60 °C, which gives access to more graphitic surface area to be oxidized.

This study has provided a broad and deep analysis of the influence of the different variables pertaining to the GrO synthesis process on the properties that most influence some of the applications sought for these materials. Applications such as hydrogen storage, water decontamination or supercapacitors require materials with high SSA and porosity,

with the % C requirement varying in each specific case. In this paper, an investigation of the relationship between the different variables of the synthesis process and the properties of the GrO obtained by the Tour method has been presented. In addition to this, the optimal conditions for the synthesis of GrO with maximum SSA and porosity have been highlighted, providing a starting point for generating high-SSA graphene aerogels in future studies for use in the aforementioned applications.

Author Contributions: Conceptualization, H.B. and M.B.G.-M.; methodology, H.B.; software, H.B.; formal analysis H.B., F.G.-P., N.B.N., L.J.B., M.Á.C. and A.V.; investigation, H.B., I.R. and M.B.G.-M.; resources, J.M., I.R. and A.J.Q.; writing—original draft preparation, H.B..; writing—review and editing, H.B., M.B.G.-M. and I.R.; supervision, M.B.G.-M. and I.R.; project administration, M.B.G.-M., J.M. and I.R. All authors have read and agreed to the published version of the manuscript.

Funding: Grants PID2020-114234RB-C21 and -C22 funded by MCIN/AEI/10.13039/501100011033; ERDF is also gratefully acknowledged for the partial funding of the XRD equipment employed in this study (Project FEDER 2004 CIEM05-34-031). A. Velasco is in receipt of an FPU grant from the Spanish Government (FPU18/03235), funded by MCIN/AEI/10.13039/501100011033 "ESF Investing in your future".

Data Availability Statement: Data are contained in Appendix A.

Conflicts of Interest: The authors declare no conflict of interest.

Appendix A

Table A1. The complete results of SSA and t-Plot-(Micropore Volume) obtained by BET from all ED experiments.

Experiment	SSA	t-Plot-(Micropore Volume)
	(m^2g^{-1})	(cm^3g^{-1})
GrO_Exp01	67.0	0.0181
GrO_Exp02	34.8	0.0009
GrO_Exp03	57.4	0.0059
GrO_Exp04	41.0	0.0041
GrO_Exp05	25.1	0.0022
GrO_Exp06	25.5	0.0021
GrO_Exp07	40.6	0.0073
GrO_Exp08	23.4	0.0022
GrO_Exp09	42.8	0.0076
GrO_Exp10	53.8	0.0078
GrO_Exp11	43.5	0.0075
GrO_Exp12	25.3	0.0022
GrO_Exp13	42.2	0.0070
GrO_Exp14	51.2	0.0082
GrO_Exp15	32.8	0.0024
GrO_Exp16	45.6	0.0080

Table A2. The complete results of C obtained by EA from all ED experiments.

Experiment	C
	(%)
GrO_Exp01	38.9
GrO_Exp02	34.6
GrO_Exp03	38.4
GrO_Exp04	42.4
GrO_Exp05	40.5
GrO_Exp06	43.1
GrO_Exp07	38.1
GrO_Exp08	36.5
GrO_Exp09	35.4
GrO_Exp10	37.6
GrO_Exp11	39.0
GrO_Exp12	39.3
GrO_Exp13	38.0
GrO_Exp14	38.0
GrO_Exp15	38.3
GrO_Exp16	37.7

Table A3. The complete results of 2θ, d-spacing, Crystal size and n obtained by XRD from all ED experiments.

Experiment	2θ	d-Spacing	Crystal Size	n
	(deg)	(nm)	(nm)	
GrO_Exp01	11.2	0.79	35.6	44.9
GrO_Exp02	10.1	0.87	58.6	67.0
GrO_Exp03	10.3	0.86	58.6	68.4
GrO_Exp04	10.5	0.84	166.1	197.7
GrO_Exp05	10.1	0.87	99.6	114.2
GrO_Exp06	9.9	0.89	76.6	86.0
GrO_Exp07	10.8	0.82	45.3	55.5
GrO_Exp08	10.1	0.88	124.6	141.7
GrO_Exp09	10.9	0.81	49.8	61.6
GrO_Exp10	10.9	0.81	33.2	40.8
GrO_Exp11	10.9	0.81	35.6	43.8
GrO_Exp12	10.1	0.87	166.0	189.9
GrO_Exp13	10.6	0.83	35.6	42.8
GrO_Exp14	10.8	0.82	27.7	33.7
GrO_Exp15	9.8	0.90	124.5	138.4
GrO_Exp16	10.8	0.82	45.3	55.1

Table A4. The complete results of I_D/I_G and I_{2D}/I_G obtained by Raman from all ED experiments.

Experiment	Raman I_D/I_G	Raman I_{2D}/I_G
GrO_Exp01	1.00	0.16
GrO_Exp02	1.02	0.17
GrO_Exp03	0.99	0.16
GrO_Exp04	0.98	0.14
GrO_Exp05	1.02	0.16
GrO_Exp06	1.00	0.18
GrO_Exp07	0.92	0.17
GrO_Exp08	1.03	0.14
GrO_Exp09	1.00	0.14
GrO_Exp10	0.90	0.13
GrO_Exp11	1.02	0.15
GrO_Exp12	0.98	0.15
GrO_Exp13	1.00	0.15
GrO_Exp14	1.01	0.16
GrO_Exp15	0.99	0.15
GrO_Exp16	0.99	0.16

References

1. Wang, C.; Kim, J.; Tang, J.; Na, J.; Kang, Y.M.; Kim, M.; Lim, H.; Bando, Y.; Li, J.; Yamauchi, Y. Large-Scale Synthesis of MOF-Derived Superporous Carbon Aerogels with Extraordinary Adsorption Capacity for Organic Solvents. *Angew. Chem. Int. Ed. Engl.* **2020**, *59*, 2066–2070. [CrossRef]
2. Czaja, A.U.; Trukhan, N.; Muller, U. Industrial applications of metal-organic frameworks. *Chem. Soc. Rev.* **2009**, *38*, 1284–1293. [CrossRef]
3. Liu, X.; Zhang, L.; Wang, J. Design strategies for MOF-derived porous functional materials: Preserving surfaces and nurturing pores. *J. Mater.* **2021**, *7*, 440–459. [CrossRef]
4. Chen, Z.; Mitchell, S.; Vorobyeva, E.; Leary, R.K.; Hauert, R.; Furnival, T.; Ramasse, Q.M.; Thomas, J.M.; Midgley, P.A.; Dontsova, D.; et al. Stabilization of Single Metal Atoms on Graphitic Carbon Nitride. *Adv. Funct. Mater.* **2017**, *27*, 1605785. [CrossRef]
5. Wang, Y.; Meng, D.; Zhao, X. Visible-light-driven H_2O_2 production from O_2 reduction with nitrogen vacancy-rich and porous graphitic carbon nitride. *Appl. Catal. B Environ.* **2020**, *273*, 119064. [CrossRef]
6. Liu, X.; Ma, R.; Wang, X.; Ma, Y.; Yang, Y.; Zhuang, L.; Zhang, S.; Jehan, R.; Chen, J.; Wang, X. Graphene oxide-based materials for efficient removal of heavy metal ions from aqueous solution: A review. *Environ. Pollut.* **2019**, *252*, 62–73. [CrossRef] [PubMed]
7. Alazmi, A.; El Tall, O.; Rasul, S.; Hedhili, M.N.; Patole, S.P.; Costa, P.M. A process to enhance the specific surface area and capacitance of hydrothermally reduced graphene oxide. *Nanoscale* **2016**, *8*, 17782–17787. [CrossRef]
8. Englert, A.H.; Rubio, J. Characterization and environmental application of a Chilean natural zeolite. *Int. J. Miner. Process.* **2005**, *75*, 21–29. [CrossRef]
9. Galarneau, A.; Mehlhorn, D.; Guenneau, F.; Coasne, B.; Villemot, F.; Minoux, D.; Aquino, C.; Dath, J.P. Specific Surface Area Determination for Microporous/Mesoporous Materials: The Case of Mesoporous FAU-Y Zeolites. *Langmuir* **2018**, *34*, 14134–14142. [CrossRef]
10. Sakthivel, T.; Reid, D.L.; Goldstein, I.; Hench, L.; Seal, S. Hydrophobic high surface area zeolites derived from fly ash for oil spill remediation. *Environ. Sci. Technol.* **2013**, *47*, 5843–5850. [CrossRef]
11. Lu, Y.; Zhan, W.; He, Y.; Wang, Y.; Kong, X.; Kuang, Q.; Xie, Z.; Zheng, L. MOF-templated synthesis of porous $Co_{(3)}O_{(4)}$ concave nanocubes with high specific surface area and their gas sensing properties. *ACS Appl. Mater. Interfaces* **2014**, *6*, 4186–4195. [CrossRef]
12. Wang, B.J.; Ma, S.Y.; Pei, S.T.; Xu, X.L.; Cao, P.F.; Zhang, J.L.; Zhang, R.; Xu, X.H.; Han, T. High specific surface area SnO_2 prepared by calcining Sn-MOFs and their formaldehyde-sensing characteristics. *Sens. Actuators B Chem.* **2020**, *321*, 128560. [CrossRef]
13. Konnerth, H.; Matsagar, B.M.; Chen, S.S.; Prechtl, M.H.G.; Shieh, F.-K.; Wu, K.C.W. Metal-organic framework (MOF)-derived catalysts for fine chemical production. *Coord. Chem. Rev.* **2020**, *416*, 213319. [CrossRef]

14. Kang, Y.-S.; Lu, Y.; Chen, K.; Zhao, Y.; Wang, P.; Sun, W.-Y. Metal–organic frameworks with catalytic centers: From synthesis to catalytic application. *Coord. Chem. Rev.* **2019**, *378*, 262–280. [CrossRef]
15. Ali Maryum, P.E.; Tayyaba, N.; Osama, R.; Rubab, Z.; Yang, M. Recent advancements in MOF-based catalysts for applications in electrochemical and photoelectrochemical water splitting: A review. *Int. J. Energy Res.* **2020**, *45*, 1190–1226. [CrossRef]
16. Qiu, B.; Xing, M.; Zhang, J. Recent advances in three-dimensional graphene based materials for catalysis applications. *Chem. Soc. Rev.* **2018**, *47*, 2165–2216. [CrossRef]
17. Pandey, A.P.; Bhatnagar, A.; Shukla, V.; Soni, P.K.; Singh, S.; Verma, S.K.; Shaneeth, M.; Sekkar, V.; Srivastava, O.N. Hydrogen storage properties of carbon aerogel synthesized by ambient pressure drying using new catalyst triethylamine. *Int. J. Hydrog. Energy* **2020**, *45*, 30818–30827. [CrossRef]
18. Gasnier, A.; Amica, G.; Juan, J.; Troiani, H.; Gennari, F.C. N-Doped Graphene-Rich Aerogels Decorated with Nickel and Cobalt Nanoparticles: Effect on Hydrogen Storage Properties of Nanoconfined $LiBH_4$. *J. Phys. Chem. C* **2019**, *124*, 115–125. [CrossRef]
19. Ferreira-Neto, E.P.; Ullah, S.; da Silva, T.C.A.; Domeneguetti, R.R.; Perissinotto, A.P.; de Vicente, F.S.; Rodrigues-Filho, U.P.; Ribeiro, S.J.L. Bacterial Nanocellulose/$MoS_{(2)}$ Hybrid Aerogels as Bifunctional Adsorbent/Photocatalyst Membranes for in-Flow Water Decontamination. *ACS Appl. Mater. Interfaces* **2020**, *12*, 41627–41643. [CrossRef]
20. Paraskevopoulou, P.; Raptopoulos, G.; Leontaridou, F.; Papastergiou, M.; Sakellari, A.; Karavoltsos, S. Evaluation of Polyurea-Crosslinked Alginate Aerogels for Seawater Decontamination. *Gels* **2021**, *7*, 27. [CrossRef]
21. Somjit, V.; Thinsoongnoen, P.; Sriphumrat, K.; Pimu, S.; Arayachukiat, S.; Kongpatpanich, K. Metal-Organic Framework Aerogel for Full pH Range Operation and Trace Adsorption of Arsenic in Water. *ACS Appl. Mater. Interfaces* **2022**, *14*, 40005–40013. [CrossRef] [PubMed]
22. Lv, Z.; Fan, Q.; Xie, Y.; Chen, Z.; Alsaedi, A.; Hayat, T.; Wang, X.; Chen, C. MOFs-derived magnetic chestnut shell-like hollow sphere NiO/Ni@C composites and their removal performance for arsenic (V). *Chem. Eng. J.* **2019**, *362*, 413–421. [CrossRef]
23. Tang, X.; Wang, S.; Zhang, Z.; Li, Z.; Wang, L.; Yuan, L.; Wang, B.; Sun, J.; Zheng, L.; Wang, H.; et al. Graphene oxide/chitosan/potassium copper hexacyanoferrate(II) composite aerogel for efficient removal of cesium. *Chem. Eng. J.* **2022**, *444*, 136397. [CrossRef]
24. Chen, L.; Feng, S.; Zhao, D.; Chen, S.; Li, F.; Chen, C. Efficient sorption and reduction of U(VI) on zero-valent iron-polyaniline-graphene aerogel ternary composite. *J. Colloid. Interface Sci.* **2017**, *490*, 197–206. [CrossRef]
25. Stoller, M.D.; Park, S.; Zhu, Y.; An, J.; Ruoff, R.S. Graphene-Based Ultracapacitors. *Nano Lett.* **2008**, *8*, 3498–3502. [CrossRef] [PubMed]
26. Soldano, C.; Mahmood, A.; Dujardin, E. Production, properties and potential of graphene. *Carbon* **2010**, *48*, 2127–2150. [CrossRef]
27. Novoselov, K.S.; Geim, A.K.; Morozov, S.V.; Jiang, D.; Zhang, Y.; Dubonos, S.V.; Grigorieva, I.V.; Firsov, A.A. Electric Field Effect in Atomically Thin Carbon Films. *Science* **2004**, *306*, 666–669. [CrossRef]
28. Wassei, J.K.; Kaner, R.B. Graphene, a promising transparent conductor. *Mater. Today* **2010**, *13*, 52–59. [CrossRef]
29. Lee, C.; Wei, X.; Kysar, J.W.; Hone, J. Measurement of the Elastic Properties and Intrinsic Strength of Monolayer Graphene. *Science* **2008**, *321*, 385–388. [CrossRef]
30. Chen, H.; Müller, M.B.; Gilmore, K.J.; Wallace, G.G.; Li, D. Mechanically Strong, Electrically Conductive, and Biocompatible Graphene Paper. *Adv. Mater.* **2008**, *20*, 3557–3561. [CrossRef]
31. Han, T.-H.; Kim, H.; Kwon, S.-J.; Lee, T.-W. Graphene-based flexible electronic devices. *Mater. Sci. Eng. R Rep.* **2017**, *118*, 1–43. [CrossRef]
32. Pinto, A.M.; Goncalves, I.C.; Magalhaes, F.D. Graphene-based materials biocompatibility: A review. *Colloids Surf. B Biointerfaces* **2013**, *111*, 188–202. [CrossRef] [PubMed]
33. Gurunathan, S.; Kim, J.H. Synthesis, toxicity, biocompatibility, and biomedical applications of graphene and graphene-related materials. *Int. J. Nanomed.* **2016**, *11*, 1927–1945. [CrossRef]
34. Hill, E.W.; Vijayaragahvan, A.; Novoselov, K. Graphene Sensors. *IEEE Sens. J.* **2011**, *11*, 3161–3170. [CrossRef]
35. Liu, J.; Cui, L.; Losic, D. Graphene and graphene oxide as new nanocarriers for drug delivery applications. *Acta Biomater.* **2013**, *9*, 9243–9257. [CrossRef]
36. Cui, G.; Bi, Z.; Zhang, R.; Liu, J.; Yu, X.; Li, Z. A comprehensive review on graphene-based anti-corrosive coatings. *Chem. Eng. J.* **2019**, *373*, 104–121. [CrossRef]
37. Peetam Mandal, J.D.; Mitali, S. A Review on the Emergence of Graphene in Photovoltaics Industry. *Biointerface Res. Appl. Chem.* **2021**, *11*, 15009–15036. [CrossRef]
38. Liao, L.; Duan, X. Graphene for radio frequency electronics. *Mater. Today* **2012**, *15*, 328–338. [CrossRef]
39. Cheng, Y.; Wang, K.; Qi, Y.; Liu, Z. Chemical Vapor Deposition Method for Graphene Fiber Materials. *Acta Phys. Chim. Sin.* **2020**, *38*, 2006046. [CrossRef]
40. Fang, B.; Chang, D.; Xu, Z.; Gao, C. A Review on Graphene Fibers: Expectations, Advances, and Prospects. *Adv. Mater.* **2020**, *32*, e1902664. [CrossRef]
41. Xu, Z.; Gao, C. Graphene fiber: A new trend in carbon fibers. *Mater. Today* **2015**, *18*, 480–492. [CrossRef]
42. Pei, S.; Zhao, J.; Du, J.; Ren, W.; Cheng, H.-M. Direct reduction of graphene oxide films into highly conductive and flexible graphene films by hydrohalic acids. *Carbon* **2010**, *48*, 4466–4474. [CrossRef]
43. Kumar, P.; Shahzad, F.; Yu, S.; Hong, S.M.; Kim, Y.-H.; Koo, C.M. Large-area reduced graphene oxide thin film with excellent thermal conductivity and electromagnetic interference shielding effectiveness. *Carbon* **2015**, *94*, 494–500. [CrossRef]

44. Paliotta, L.; De Bellis, G.; Tamburrano, A.; Marra, F.; Rinaldi, A.; Balijepalli, S.K.; Kaciulis, S.; Sarto, M.S. Highly conductive multilayer-graphene paper as a flexible lightweight electromagnetic shield. *Carbon* **2015**, *89*, 260–271. [CrossRef]
45. Cao, J.; Wang, Y.; Xiao, P.; Chen, Y.; Zhou, Y.; Ouyang, J.-H.; Jia, D. Hollow graphene spheres self-assembled from graphene oxide sheets by a one-step hydrothermal process. *Carbon* **2013**, *56*, 389–391. [CrossRef]
46. Xiao, W.; Zhang, Y.; Tian, L.; Liu, H.; Liu, B.; Pu, Y. Facile synthesis of reduced graphene oxide/titania composite hollow microspheres based on sonication-assisted interfacial self-assembly of tiny graphene oxide sheets and the photocatalytic property. *J. Alloys Compd.* **2016**, *665*, 21–30. [CrossRef]
47. Huang, X.; Yu, G.; Zhang, Y.; Zhang, M.; Shao, G. Design of cellular structure of graphene aerogels for electromagnetic wave absorption. *Chem. Eng. J.* **2021**, *426*, 131894. [CrossRef]
48. Wei, L.; Mao, Y. Enhanced hydrogen storage performance of reduced graphene oxide hybrids with nickel or its metallic mixtures based on spillover mechanism. *Int. J. Hydrog. Energy* **2016**, *41*, 11692–11699. [CrossRef]
49. Du, J.; Liu, L.; Yu, Y.; Zhang, L.; Zhang, Y.; Chen, A. Synthesis of nitrogen doped graphene aerogels using solid supported strategy for supercapacitor. *Mater. Chem. Phys.* **2019**, *223*, 145–151. [CrossRef]
50. Nandanapalli, K.R.; Mudusu, D.; Lee, S. Functionalization of graphene layers and advancements in device applications. *Carbon* **2019**, *152*, 954–985. [CrossRef]
51. Zhang, Y.; Wan, Q.; Yang, N. Recent Advances of Porous Graphene: Synthesis, Functionalization, and Electrochemical Applications. *Small* **2019**, *15*, e1903780. [CrossRef]
52. Lee, S.J.; Theerthagiri, J.; Nithyadharseni, P.; Arunachalam, P.; Balaji, D.; Madan Kumar, A.; Madhavan, J.; Mittal, V.; Choi, M.Y. Heteroatom-doped graphene-based materials for sustainable energy applications: A review. *Renew. Sustain. Energy Rev.* **2021**, *143*, 110849. [CrossRef]
53. Fang, Q.; Shen, Y.; Chen, B. Synthesis, decoration and properties of three-dimensional graphene-based macrostructures: A review. *Chem. Eng. J.* **2015**, *264*, 753–771. [CrossRef]
54. Zhu, C.; Han, T.Y.; Duoss, E.B.; Golobic, A.M.; Kuntz, J.D.; Spadaccini, C.M.; Worsley, M.A. Highly compressible 3D periodic graphene aerogel microlattices. *Nat. Commun.* **2015**, *6*, 6962. [CrossRef]
55. Xu, Y.; Sheng, K.; Li, C.; Shi, G. Self-Assembled Graphene Hydrogel via a One-Step Hydrothermal Process. *ASC Nano* **2010**, *4*, 4324–4330. [CrossRef] [PubMed]
56. Garcia-Bordejé, E.; Benito, A.M.; Maser, W.K. Graphene aerogels via hydrothermal gelation of graphene oxide colloids: Fine-tuning of its porous and chemical properties and catalytic applications. *Adv. Colloid. Interface Sci.* **2021**, *292*, 102420. [CrossRef] [PubMed]
57. Rodríguez-Mata, V.; González-Domínguez, J.M.; Benito, A.M.; Maser, W.K.; García-Bordejé, E. Reduced Graphene Oxide Aerogels with Controlled Continuous Microchannels for Environmental Remediation. *ACS Appl. Nano Mater.* **2019**, *2*, 1210–1222. [CrossRef]
58. Gómez-Mancebo, M.B.; Fernández-Martínez, R.; Ruiz-Perona, A.; Rubio, V.; Bastante, P.; García-Pérez, F.; Borlaf, F.; Sánchez, M.; Hamada, A.; Velasco, A.; et al. Comparison of Thermal and Laser-Reduced Graphene Oxide Production for Energy Storage Applications. *Nanomaterials* **2023**, *13*, 1391. [CrossRef]
59. Wang, C.; Han, X.; Xu, P.; Zhang, X.; Du, Y.; Hu, S.; Wang, J.; Wang, X. The electromagnetic property of chemically reduced graphene oxide and its application as microwave absorbing material. *Appl. Phys. Lett.* **2011**, *98*, 072906. [CrossRef]
60. Zhang, H.; Luo, N.; Liu, T.; Chen, F.; Fu, Q. Light-weight, low-loading and large-sheet reduced graphene oxide for high-efficiency microwave absorber. *Carbon* **2022**, *196*, 1024–1034. [CrossRef]
61. Wang, S.; Zhao, Y.; Gao, M.; Xue, H.; Xu, Y.; Feng, C.; Shi, D.; Liu, K.; Jiao, Q. Green Synthesis of Porous Cocoon-like rGO for Enhanced Microwave-Absorbing Performances. *ACS Appl. Mater. Interfaces* **2018**, *10*, 42865–42874. [CrossRef]
62. Ye, S.; Liu, Y.; Feng, J. Low-Density, Mechanical Compressible, Water-Induced Self-Recoverable Graphene Aerogels for Water Treatment. *ACS Appl. Mater. Interfaces* **2017**, *9*, 22456–22464. [CrossRef]
63. Wang, C.; Chen, X.; Wang, B.; Huang, M.; Wang, B.; Jiang, Y.; Ruoff, R.S. Freeze-Casting Produces a Graphene Oxide Aerogel with a Radial and Centrosymmetric Structure. *ACS Nano* **2018**, *12*, 5816–5825. [CrossRef] [PubMed]
64. Agarwal, V.; Zetterlund, P.B. Strategies for reduction of graphene oxide—A comprehensive review. *Chem. Eng. J.* **2021**, *405*, 127018. [CrossRef]
65. De Silva, K.K.H.; Huang, H.-H.; Joshi, R.; Yoshimura, M. Restoration of the graphitic structure by defect repair during the thermal reduction of graphene oxide. *Carbon* **2020**, *166*, 74–90. [CrossRef]
66. De Silva, K.K.H.; Huang, H.H.; Joshi, R.K.; Yoshimura, M. Chemical reduction of graphene oxide using green reductants. *Carbon* **2017**, *119*, 190–199. [CrossRef]
67. McGrail, B.T.; Rodier, B.J.; Pentzer, E. Rapid Functionalization of Graphene Oxide in Water. *Chem. Mater.* **2014**, *26*, 5806–5811. [CrossRef]
68. Zhang, D.-D.; Zu, S.-Z.; Han, B.-H. Inorganic–organic hybrid porous materials based on graphite oxide sheets. *Carbon* **2009**, *47*, 2993–3000. [CrossRef]
69. Stankovich, S.; Dikin, D.A.; Piner, R.D.; Kohlhaas, K.A.; Kleinhammes, A.; Jia, Y.; Wu, Y.; Nguyen, S.T.; Ruoff, R.S. Synthesis of graphene-based nanosheets via chemical reduction of exfoliated graphite oxide. *Carbon* **2007**, *45*, 1558–1565. [CrossRef]
70. Zhu, W.; Lin, Y.; Kang, W.; Quan, H.; Zhang, Y.; Chang, M.; Wang, K.; Zhang, M.; Zhang, W.; Li, Z.; et al. An aerogel adsorbent with bio-inspired interfacial adhesion between graphene and MoS2 sheets for water treatment. *Appl. Surf. Sci.* **2020**, *512*, 145717. [CrossRef]

71. Xu, J.; Du, P.; Bi, W.; Yao, G.; Li, S.; Liu, H. Graphene oxide aerogels co-functionalized with polydopamine and polyethylenimine for the adsorption of anionic dyes and organic solvents. *Chem. Eng. Res. Des.* **2020**, *154*, 192–202. [CrossRef]
72. Brodie, B.C. On the Atomic Weight of Graphite. *Philos. Trans. R. Soc. Lond.* **1859**, *149*, 249–259. [CrossRef]
73. Staudenmaier, L. Verfahren zur Darstellung der Graphitsäure. *Ber. Der Dtsch. Chem. Ges.* **1898**, *31*, 1481–1487. [CrossRef]
74. William, S.; Hummers, J.; Richard, E. Offeman. Preparation of Graphitic Oxide. *J. Am. Chem. Soc.* **1958**, *80*, 1339. [CrossRef]
75. Habte, A.T.; Ayele, D.W. Synthesis and Characterization of Reduced Graphene Oxide (rGO) Started from Graphene Oxide (GO) Using the Tour Method with Different Parameters. *Adv. Mater. Sci. Eng.* **2019**, *2019*, 5058163. [CrossRef]
76. Deemer, E.M.; Paul, P.K.; Manciu, F.S.; Botez, C.E.; Hodges, D.R.; Landis, Z.; Akter, T.; Castro, E.; Chianelli, R.R. Consequence of oxidation method on graphene oxide produced with different size graphite precursors. *Mater. Sci. Eng. B.* **2017**, *224*, 150–157. [CrossRef]
77. Marcano, D.C.; Kosynkin, D.V.; Berlin, J.M.; Sinitskii, A.; Sun, Z.; Slesarev, A.; Alemany, L.B.; Lu, W.; Tour, J.M. Improved Synthesis of Graphene Oxide. *ACS Nano* **2010**, *4*, 4806–4814. [CrossRef]
78. Hou, Y.; Lv, S.; Liu, L.; Liu, X. High-quality preparation of graphene oxide via the Hummers' method: Understanding the roles of the intercalator, oxidant, and graphite particle size. *Ceram. Int.* **2020**, *46*, 2392–2402. [CrossRef]
79. Peng, S.; Fan, X.; Li, S.; Zhang, J. Green Synthesis and Characterization of Graphite Oxide by Orthogonal Experiment. *J. Chil. Chem. Soc.* **2013**, *58*, 2213–2217. [CrossRef]
80. Kumar, S.; Baruah, B.; Kumar, A. Tunable degree of oxidation through variation of H_2O_2 concentration and its effect on structural, optical and supercapacitive properties of graphene oxide powders synthesized using improved method. *Mater. Today Commun.* **2017**, *13*, 26–35. [CrossRef]
81. Charpy, G. Lur Sar Formation de L'oxyde Graphitique et la Définition du Graphite. *Comptes Rendus Hebd. Des. Seances De. L Acad. Des. Sci.* **1909**, *148*, 920–923.
82. Koch, K.R. Oxidation by Mn207: An impressive demonstration of the powerful oxidizing property of dimanganeseheptoxide. *J. Chem. Educ.* **1982**, *59*, 973. [CrossRef]
83. Fatmawati, D.A.; Triyono, T.; Trisunaryanti, W.; Oktaviano, H.S.; Chasanah, U. The Influence of Permanganate Enhancement to Graphite on Chemical Structure and Properties of Graphene Oxide Material Generated by Improved Tour Method. *Indones. J. Chem.* **2021**, *21*, 1086. [CrossRef]
84. Emiru, T.F.; Ayele, D.W. Controlled synthesis, characterization and reduction of graphene oxide: A convenient method for large scale production. *Egypt. J. Basic. Appl. Sci.* **2019**, *4*, 74–79. [CrossRef]
85. Rao, K.S.; Senthilnathan, J.; Liu, Y.F.; Yoshimura, M. Role of peroxide ions in formation of graphene nanosheets by electrochemical exfoliation of graphite. *Sci. Rep.* **2014**, *4*, 4237. [CrossRef]
86. Eigler, S.; Grimm, S.; Hof, F.; Hirsch, A. Graphene oxide: A stable carbon framework for functionalization. *J. Mater. Chem. A* **2013**, *1*, 11559. [CrossRef]
87. Morimoto, N.; Suzuki, H.; Takeuchi, Y.; Kawaguchi, S.; Kunisu, M.; Bielawski, C.W.; Nishina, Y. Real-Time, in Situ Monitoring of the Oxidation of Graphite: Lessons Learned. *Chem. Mater.* **2017**, *29*, 2150–2156. [CrossRef]
88. Eigler, S.; Hirsch, A. Chemistry with graphene and graphene oxide-challenges for synthetic chemists. *Angew. Chem. Int. Ed. Engl.* **2014**, *53*, 7720–7738. [CrossRef]
89. Lavin-Lopez, M.D.; Romero, A.; Garrido, J.; Sanchez-Silva, L.; Valverde, J.L. Influence of Different Improved Hummers Method Modifications on the Characteristics of Graphite Oxide in Order to Make a More Easily Scalable Method. *Ind. Eng. Chem. Res.* **2016**, *55*, 12836–12847. [CrossRef]
90. Velasco-Hernández, A.; Esparza-Muñoz, R.A.; de Moure-Flores, F.J.; Santos-Cruz, J.; Mayén-Hernández, S.A. Synthesis and characterization of graphene oxide—TiO_2 thin films by sol-gel for photocatalytic applications. *Mater. Sci. Semicond. Process.* **2020**, *114*, 105082. [CrossRef]
91. Krishnamoorthy, K.; Veerapandian, M.; Yun, K.; Kim, S.J. The chemical and structural analysis of graphene oxide with different degrees of oxidation. *Carbon* **2013**, *53*, 38–49. [CrossRef]
92. Eigler, S.; Dotzer, C.; Hirsch, A.; Enzelberger, M.; Müller, P. Formation and Decomposition of CO_2 Intercalated Graphene Oxide. *Chem. Mater.* **2012**, *24*, 1276–1282. [CrossRef]
93. Patterson, A.L. The Scherrer Formula for X-Ray Particle Size Determination. *Phys. Rev.* **1939**, *56*, 978–982. [CrossRef]
94. Lerf, A.; Buchsteiner, A.; Pieper, J.; Schöttl, S.; Dekany, I.; Szabo, T.; Boehm, H.P. Hydration behavior and dynamics of water molecules in graphite oxide. *J. Phys. Chem. Solids* **2006**, *67*, 1106–1110. [CrossRef]
95. Rezania, B.; Severin, N.; Talyzin, A.V.; Rabe, J.P. Hydration of Bilayered Graphene Oxide. *Nano Lett.* **2014**, *14*, 3993–3998. [CrossRef]
96. Liu, L.; Zhang, R.; Liu, Y.; Tan, W.; Zhu, G. Insight into hydrogen bonds and characterization of interlayer spacing of hydrated graphene oxide. *J. Mol. Model.* **2018**, *24*, 137. [CrossRef]
97. Kim, D.; Kim, D.W.; Lim, H.-K.; Jeon, J.; Kim, H.; Jung, H.-T.; Lee, H. Intercalation of Gas Molecules in Graphene Oxide Interlayer: The Role of Water. *J. Phys. Chem. C* **2014**, *118*, 11142–11148. [CrossRef]
98. Kaniyoor, A.; Ramaprabhu, S. A Raman spectroscopic investigation of graphite oxide derived graphene. *AIP Adv.* **2012**, *2*, 032183. [CrossRef]
99. Tojo, T.; Shinohara, M.; Fujisawa, K.; Muramatsu, H.; Hayashi, T.; Kim, Y.A.; Endo, M. Highly Conductive One-Dimensional Manganese Oxide Wires by Coating with Graphene Oxides. *Appl. Phys. Express* **2012**, *5*, 105001. [CrossRef]

100. Sharma, M.; Rani, S.; Pathak, D.K.; Bhatia, R.; Kumar, R.; Sameera, I. Temperature dependent Raman modes of reduced graphene oxide: Effect of anharmonicity, crystallite size and defects. *Carbon.* **2021**, *184*, 437–444. [CrossRef]
101. Nguyen, V.T.; Le, H.D.; Nguyen, V.C.; Tam Ngo, T.T.; Le, D.Q.; Nguyen, X.N.; Phan, N.M. Synthesis of multi-layer graphene films on copper tape by atmospheric pressure chemical vapor deposition method. *Adv. Nat. Sci. Nanosci. Nanotechnol.* **2013**, *4*, 035012. [CrossRef]